JOURNAL OF THERMOPHYSICS AND HEAT TRANSFER
Vol. 24, No. 1, January–March 2010

Unsteady Simulations of a Film Cooling Flow from an Inclined Cylindrical Jet

Sung In Kim* and Ibrahim Hassan†
Concordia University, Montreal, Quebec H3G 1M8, Canada

DOI: 10.2514/1.33167

Film cooling is extensively used to provide protection against the severe thermal environment in gas turbine engines. Most of the computational studies on film cooling flow have been done using steady Reynolds-averaged Navier–Stokes calculation procedures. However, the flowfield associated with a jet in a crossflow is highly unsteady and complex with different types of vortical structures. In this paper, a computational investigation about the unsteady phenomena of a jet in a crossflow is performed using detached eddy simulation. Detailed computation of a single row of 35 deg round holes on a flat plate has been obtained for a 1.0 blowing ratio and a 2.0 density ratio. First, time-step size, grid resolution, and computational domain tests for an unsteady simulation have been conducted. Comparison between the results of unsteady Reynolds-averaged Navier–Stokes calculation, detached eddy simulation, and large eddy simulation is also performed. Comparison of the time-averaged detached eddy simulation prediction with the measured film-cooling effectiveness shows that the detached eddy simulation prediction is reasonable. From present detached eddy simulations, the influential coherent vortical structures of a film cooling flow can be seen. The unsteady physics of jet in a crossflow interactions and a jet liftoff in film cooling flows have been explained.

Nomenclature

d	=	diameter of the cylindrical hole, m
d_w	=	distance from the wall
m	=	blowing ratio, $\rho_j U_j/\rho_\infty U_\infty$
Q	=	normalized Q criterion, $q(d/U_\infty)^2$
q	=	Q criterion, $(\lvert\Omega_{ij}\rvert^2\text{-}\lvert S_{ij}\rvert^2)/2$
U	=	velocity, m/s
x	=	streamwise coordinate, m
y	=	vertical coordinate, m
y^+	=	nondimensional wall distance, $\rho u_\tau y_p/\mu$
z	=	spanwise coordinate, m
η	=	adiabatic film-cooling effectiveness, $(T_{\text{aw}}\text{-}T_\infty)/(T_j\text{-}T_\infty)$
θ	=	nondimensional temperature, $(T - T_j)/(T_\infty - T_j)$
ρ	=	density, kg/m^3
Ω	=	vorticity, 1/s
ω	=	normalized vorticity, $\Omega(d/U_\infty)$

Subscripts

aw	=	adiabatic wall
j	=	refers to the jet
w	=	wall conditions
∞	=	mainstream conditions at inlet plane and in freestream

Introduction

ADVANCED gas turbine engines adopt a higher turbine inlet temperature to achieve a higher turbine power output. The higher turbine inlet temperature requires more effective turbine cooling strategies. Film cooling has been extensively used to provide the protection of the turbine material from the severe thermal environment. A lot of experimental and computational studies have been conducted with regard to the film-cooling characteristics of turbine blades. In film cooling, coolant jets are issued with an angle into the hot crossflow and deflected over the target surface to provide coolant film coverage. However, film cooling causes a reduction of the air in the main flowpath through the combustor, and coolant injection induces additional aerodynamic losses. Over the past decades, significant effort has been devoted to minimize coolant usage and maximize cooling effectiveness. The fundamental research of a jet in a crossflow is still being carried out, because this jet in a crossflow is not yet fully understood. To design a more effective cooling system, a complete understanding of the complex flow and heat transfer characteristics associated with the cooling jet–crossflow interaction is required.

Most previous computational studies on film cooling flows have been done using steady Reynolds-averaged Navier–Stokes computations [1–5]. However, experimental results [6,7] showed that the flowfield associated with a jet in a crossflow is highly unsteady and complex with different types of vortical structures. The inherent unsteadiness of the coolant jet–crossflow interactions may have important implications on the cooling performance. In general, steady RANS (Reynolds-averaged Navier–Stokes) calculations underpredict the lateral spread and mixing of the jet, whereas they overpredict the film-cooling effectiveness in the near field of the coolant injection for high blowing ratios. RANS modeling either at the two-equation level or at the second-moment level inaccurately predicted the turbulent stresses and the scalar mixing [8]. A detailed study on inherent unsteady features of the film cooling flow is rather rare. Recently, several studies on unsteady features of the film cooling flow have been attempted using LES (large eddy simulation) or DES (detached eddy simulation) schemes.

Tyagi and Acharya [9] adopted a LES scheme in order to capture unsteadiness in the flows and reported the large-scale unsteady dynamics of the coolant jet–crossflow interaction for an inclined film-cooling jet. Their prediction of the film-cooling effectiveness at a low blowing ratio of 0.5 shows a good agreement with the experimental data. Rozati and Tafti [10] investigated film cooling for a cylindrical leading edge using LES. They presented the effect of blowing ratios (0.4 and 0.8) on the influential coherent structures, film-cooling effectiveness, and the span coverage of the coolant. LES predicted well the unsteady vortical structures in film cooling flows and film-cooling effectiveness at low blowing ratios. However, the

Received 30 June 2007; revision received 2 June 2008; accepted for publication 4 June 2008.

*Research Associate, Department of Mechanical and Industrial Engineering; sikim@alcor.concordia.ca. Member AIAA.
†Associate Professor, Department of Mechanical and Industrial Engineering; ibrahimh@alcor.concordia.ca.

good agreement of film-cooling effectiveness at high blowing ratios using LES has not yet been reported in literature.

DES [11] is intended to combine the advantages of LES and RANS models. Roy et al. [12] presented the first detached eddy simulation of a film cooling flow. They investigated a single row of 35 deg round holes on a flat plate for a blowing ratio of 1.0. The results indicate a highly anisotropic mixing process downstream of the hole. However, the discrepancy between the laterally-averaged film-cooling effectiveness of the experiments and their DES prediction was identified. This discrepancy is partly attributed to the use of a symmetry boundary condition, considering just half of the film-cooling hole configuration.

Martini et al. [13] performed the unsteady flow simulation of the trailing-edge film cooling on the pressure-side cutback of gas turbine airfoils using DES. The DES simulations gave detailed insight into the unsteady film mixing process on the trailing-edge cutback, which is indeed influenced by vortex shedding from the pressure-side lip. Furthermore, the time-averaged DES results show very good agreement with the experimental data in terms of film-cooling effectiveness and heat transfer coefficients.

In this paper, a computational investigation about the unsteady phenomena of a film cooling flow has been performed using a detached eddy simulation scheme. Detailed computation of a single row of 35 deg round holes on a flat plate has been obtained for a blowing ratio of $m = 1.0$ and a density ratio of 2.0 ρ_j/ρ_∞. To obtain the accurate unsteady three-dimensional simulations, time-step size, grid resolution, computational domains, and unsteady turbulence models tests have been conducted. Comparison of the time-averaged DES prediction with the measured film-cooling effectiveness was also performed. The unsteady physics of the jet in a crossflow interactions and a jet liftoff in film cooling flows have been explored.

DES Turbulence Modeling

The complex, dynamic nature of a film cooling flow makes it necessary to model the vortices using temporally and spatially accurate calculation of the flowfield. Direct numerical simulation (DNS) is considered as the most accurate simulation. However, DNS explicitly accounts for all scales of motion in a turbulent flow using a very fine grid. DNS requires a lot of grid points, and the applicability of DNS has a limitation in high Reynolds-number flows [14,15]. Large eddy simulation is also quite reliable to resolve unsteady turbulent flows. In LES, the large-scale structure of turbulent flow is computed directly, and the smallest and nearly isotropic eddies are modeled as subgrid-scale eddies. Although LES requires less computational effort or can simulate flows at higher a Reynolds number than DNS, one major challenge for performing LES in film cooling is the range of length scales that must be resolved in the computation [16]. Based on the scales, LES remains very expensive [12,17]. As a viable alternative, this paper presents the application of detached eddy simulation to a film cooling flow.

Detached eddy simulation is a hybrid model that combines the efficiency of RANS and the accuracy of LES length scales to work under a single framework. In the DES approach, the unsteady RANS models are employed in the near-wall regions, such as inside the numerically-predicted boundary layer. The LES region is normally associated with the core turbulent region, where large turbulence scales play a dominant role. In the regions far from the wall, the DES models recover the respective subgrid models, and the length scale becomes grid dependent. DES works by applying a variable length scale that varies as a function of the distance to the nearest wall in the attached boundary layer and conforms with a subgrid scale in the rest of the flow, including separated regions and near wake [18].

The Spalart–Allmaras-based (S–A) DES model and the realizable k-ε-based (RKE) DES model are used in the present study. The Spalart–Allmaras model is a relatively simple one-equation model that solves a modeled transport equation for the kinematic eddy (turbulent) viscosity. The Spalart–Allmaras model was designed specifically for aerospace applications involving wall-bounded flows and has been shown to give good results for boundary layers subjected to adverse pressure gradients. The standard Spalart–Allmaras model uses the distance to the closest wall as the definition for the length scale l, which plays a major role in determining the level of production and destruction of turbulent viscosity [19]. The DES model replaces l everywhere with a new length scale d_w, defined as

$$d_w = \min(l, C_{\text{des}}\Delta)$$

where the grid spacing Δ is based on the largest grid space in the x, y, or z directions forming the computational cell. The empirical constant C_{des} has a value of 0.65 [20].

The realizable k-ε model is a relatively recent development. The realizable k-ε model contains a new formulation for the turbulent viscosity. A new transport equation for the dissipation rate ε has been derived from an exact equation for the transport of the mean-square vorticity fluctuation. An immediate benefit of the realizable k-ε model is that it more accurately predicts the spreading rate of both planar and round jets. It is also likely to provide superior performance for flows involving rotation, boundary layers under strong adverse pressure gradients, separation, and recirculation [21]. In the realizable k-ε-based DES model, the RANS model is similar to the realizable k-ε model with the exception of the dissipation term Y_k in the k equation. In the DES model, the realizable k-ε dissipation term is modified such that

$$Y_k = \frac{\rho k^{\frac{3}{2}}}{l_{\text{des}}}$$

where

$$l_{\text{des}} = \min(l_{\text{rke}}, l_{\text{les}}), \qquad l_{\text{rke}} = \frac{k^{\frac{3}{2}}}{\varepsilon}, \qquad l_{\text{les}} = C_{\text{des}}\Delta$$

where C_{des} is a calibration constant used in the DES model and has a value of 0.61 and Δ is the maximum local grid spacing (Δx, Δy, Δz) [20].

Numerical Approach

All simulations have been performed using the Fluent 6.3 software from Fluent, Inc. This software is run using the pressure–velocity correction with the SIMPLE algorithm. The momentum equations are discretized with bounded central differencing, which is recommended for LES/DES schemes. Other spatial discretizations are done using the second-order upwind scheme. The temporal differencing is done using the second-order implicit scheme.

Computational Domains

The computational domain of interest is shown in Fig. 1 and represents half of a spanwise periodic module containing a single coolant delivery tube inclined at 35 deg in the streamwise direction and a coolant plenum chamber. The test conditions are based on the

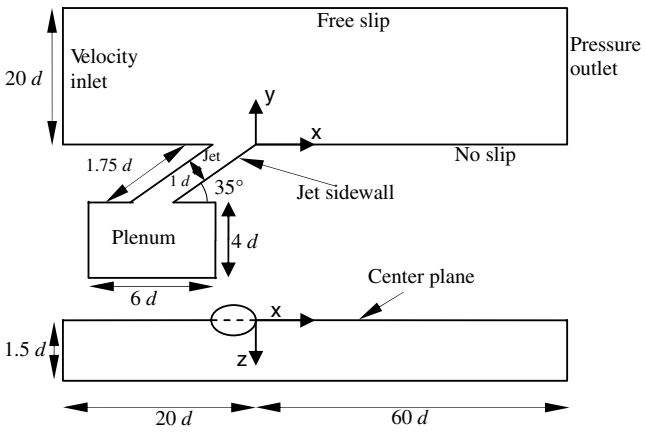

Fig. 1 Schematic of the computational domain and boundary conditions.

study from Sinha et al. [22]. The cool jet at a temperature of $T_j = 150$ K is injected into the hot freestream of $T_\infty = 300$ K. The mainstream flow condition is kept constant with $U_\infty = 20$ m/s at the inlet. The blowing ratio is achieved by changing the plenum inlet mass flow rate. The uniform velocity profile with a 0.2% turbulence level is imposed at both the mainstream and plenum inlet boundaries. The injection hole is a circular pipe with a diameter of $d = 1.27$ cm. The Reynolds number based on the hole diameter is 16,200. For this geometry, film-cooling effectiveness measurements have been provided by [22] with a coolant delivery tube length of 1.75 d. The DES results of the present study are compared with this reported measurement. The origin of the coordinate system is set at the trailing edge of the jet outlet. At the upstream inlet $x/d = -20$ a velocity inlet condition is applied. At the outlet $x/d = 60$ a pressure boundary condition is applied. The domain extends vertically to $y/d = 20$ from the bottom test surface $y = 0$, far enough such that a free-slip boundary condition or zero shear stress may be applied. From the previous work of Zhang and Hassan [5] it is known that the selection of the computational domain is important. And the height of 20 d is suitable for the computational study of this flow. The computational domain is symmetric about the central plane. Thus, symmetry boundary conditions could be imposed at both the central plane and the $z/d = 1.5$ plane in the spanwise direction for using the half-computational domain. In contrast with the geometry, the film cooling flow may show an asymmetric behavior due to the unsteadiness and the anisotropic turbulence. In this study, unsteady simulations are performed using both half and full computational domains. The discrepancy between them is compared. For the full computational domain, a periodic boundary condition is applied at the $z/d = \pm 1.5$ planes in the spanwise direction. At the bottom wall as well as the other walls an adiabatic wall boundary condition with no-slip is imposed.

Grid Test

A multiblock computational grid was developed using GAMBIT. The mesh consisted of three blocks, and they were combined with an interface boundary type at the inlet and exit of the injection hole. A structured mesh was applied to the crossflow (mainstream) block as well as the plenum block, whereas the volume of the injection pipe had an unstructured mesh. A close-up of the center-plane view of the mesh near the injection pipe region is shown in Fig. 2. This mesh was created to resolve the features of the flowfield with most of the cells concentrated in areas of large variable gradients. When used appropriately, the method successfully captured the jet liftoff effect in traditional circular jet in a crossflow over a flat plate. Details of this methodology can be found in [5]. It should be noted that this is only for the steady numerical study (realizable k-ε model used) clearly demonstrating the successful capturing of the jet liftoff effect in the circular hole on a flat plate. However, the effectiveness in the spanwise direction and the laterally-averaged effectiveness at the downstream region were less than the experiments. It was one of the motivations for the present unsteady simulations. This numerical

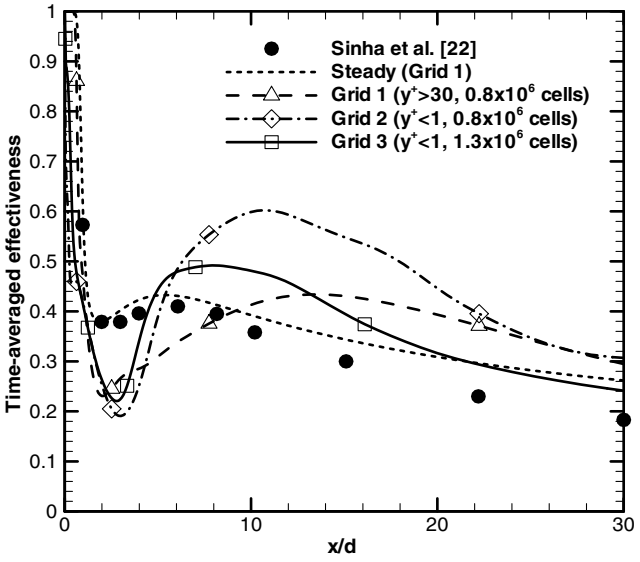

Fig. 3 Grid test with time-averaged film-cooling effectiveness along the centerline.

procedure was extended to study film cooling flows with unsteady DES simulation.

The first trial mesh (grid 1) was created with about 0.8×10^6 cells, based on previous steady work [5]. The wall y^+ value of the turbulence properties of the first mesh was about 30. To resolve the unsteady boundary layer appropriately using the DES scheme, the y^+ value of the first cell from the wall was decreased less than unity (grid 2; $y^+ < 1$ and about 0.8×10^6 cells). The predictions of the film-cooling effectiveness for different grids using the RKE-based DES model are shown in Fig. 3. The sudden decrease of film-cooling effectiveness due to jet lift was better predicted by grid 2. However, it still showed a large discrepancy with measurement. So, the total cells of the mesh were increased in order to capture the detailed vortical structure in the wake region of the coolant jet. Grid 3 (about 1.3×10^6 cells) shows better results than others. In grid 3, the value of the near-wall step, the stretching factor of the wall-normal grid, and the typical number of cells in the jet shear layer were $\Delta y^+ = 0.32$, $\Delta y_{j+1}/\Delta y_j = 1.14$, and 0.39×10^6, respectively. It was within the range of the guidelines for DES grids [23]. More cells may lead to a better solution, however, the required computing resource and time significantly increases. Therefore, grid 3 ($y^+ < 1$, about 1.3×10^6 cells) is selected in the present study.

Time-Step Refinement

Choice of the time-step size is an important factor in unsteady flow analysis. Obviously, the choice of time step affects the maximum and minimum frequencies that can be resolved in the flow. We have tested several time steps, including $T1(\Delta t = 1 \times 10^{-4}$ s),

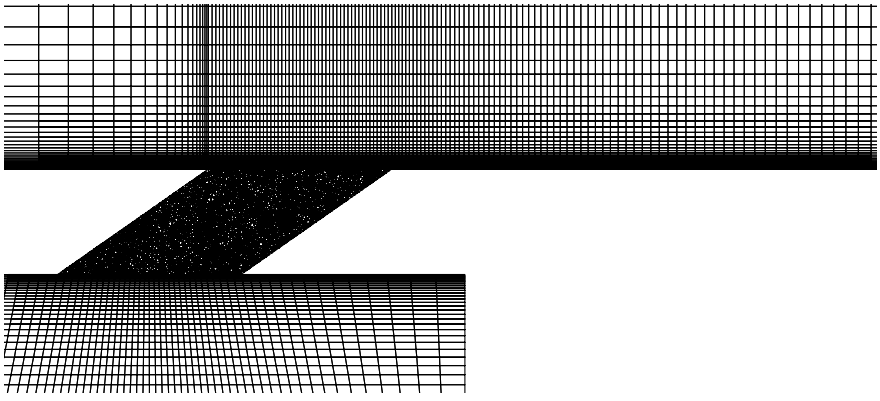

Fig. 2 Close-up of the center-plane view of the selected mesh near the injection region.

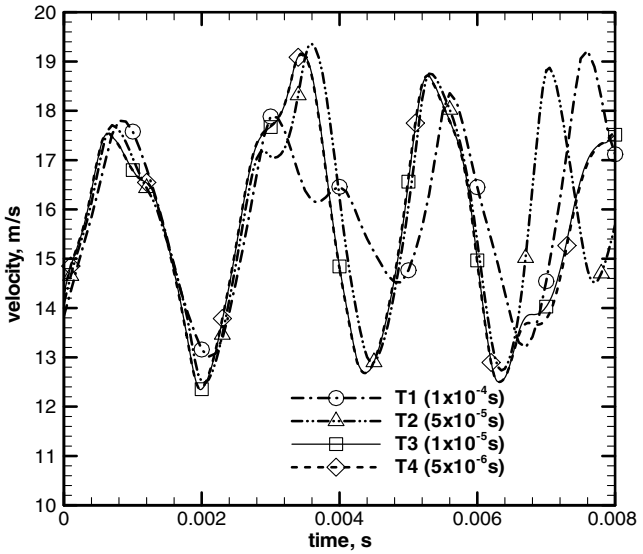

Fig. 4 An example of u-velocity time histories at a point (7.5, 1.18, and 0.0 d) for various time steps with a full domain.

$T2(\Delta t = 5 \times 10^{-5}\ \mathrm{s})$, $T3(\Delta t = 1 \times 10^{-5}\ \mathrm{s})$, and $T4(\Delta t = 5 \times 10^{-6}\ \mathrm{s})$. Figure 4 shows an example of the computed u velocity histories at a point (7.5, 1.18, and 0.0 d) for various time steps using a full domain. It is seen that the discrepancy between values, such as the amplitude, the frequency, and the mean value of the velocity fluctuation, is reduced as the time-step size is reduced. We thus conclude that the time step $T3$ ($\Delta t = 1 \times 10^{-5}\ \mathrm{s} = 0.00787\ d/U_\infty$) is capable of capturing the unsteady features of the flow and must be sufficient. Hence, $T3$ is used throughout the present computations.

Convergence within an individual time step has been achieved by using an appropriate combination of time-step size and number of subiterations per time step. In each time step, subiterations were carried out until the solution residual dropped at least 3 orders of magnitude, which proved sufficient for general unsteady flow solutions. The error of the net balances of mass and energy per each time step with 30 iterations are less than 0.1% and 1.0%, respectively. As a result, 30 iterations per time step are adequate.

Effect of Lateral Extent of Computational Domains

Symmetric boundary conditions are employed in the spanwise direction at the center plane and $z/d = 1.5$ plane when a half-domain is used. The use of the symmetry boundary condition in the spanwise direction can be considered as a limitation of the unsteady simulation as it prevents the possibility of capturing the unsteady asymmetric vortical flow patterns. The large-scale structures convecting downstream may induce the three-dimensional instability waves. Therefore, unsteady simulations using both a half-domain with symmetry boundary conditions and a full domain have been performed. The results are compared with each other.

Instantaneous temperature contours and corresponding velocity vector distributions at the $x/d = 5$ plane in the streamwise direction are shown in Fig. 5. Both sides of the symmetric line are plotted to depict the dominant bound vortical structure for the case with a half-domain (Fig. 5a). Figure 5b shows that those of the case with a full domain are somewhat asymmetric in nature, in contrast to the case with a half-domain. The coolant of the case with a full domain also exhibits unsteady spanwise fluctuations (see Fig. 6), whereas the computation with a half-domain could not capture the fluctuating distribution in the spanwise direction. Figure 7 depicts the comparison of time-averaged spanwise film-cooling effectiveness at $x/d = 15$ for both cases of a half-domain and a full domain. By comparing the width of the coolant spread, the computation with a full domain predicts a wider time-averaged footprint than that of a half-domain. This result shows that the unsteady simulation with a full domain is required to accurately predict lateral spreading of the

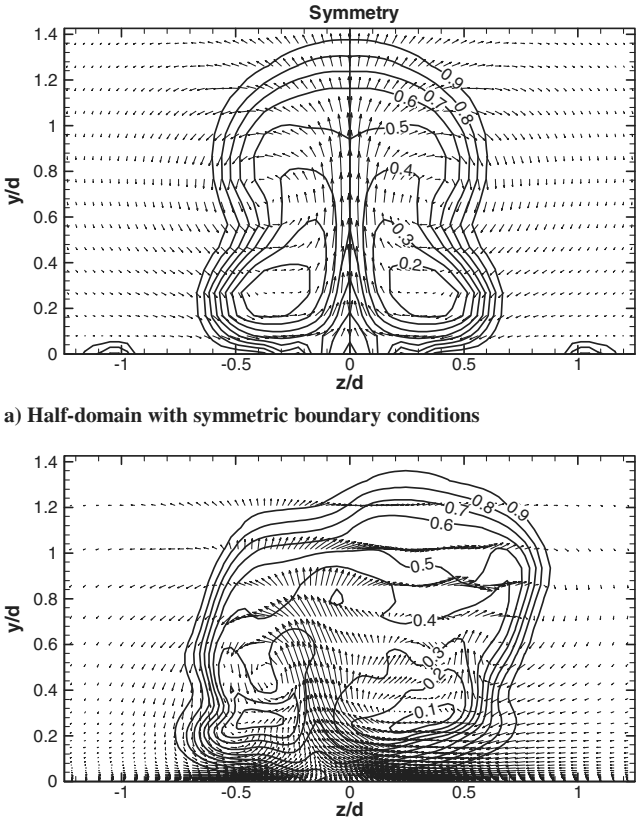

a) Half-domain with symmetric boundary conditions

b) Full domain with periodic boundary conditions

Fig. 5 Instantaneous temperature (θ) contours and velocity vectors at $x/d = 5$ plane.

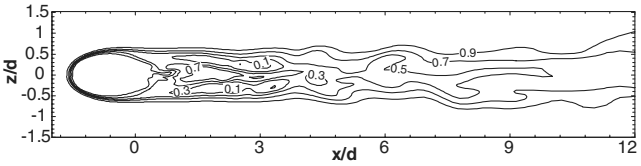

Fig. 6 Instantaneous temperature (θ) distribution at $y/d = 0.1$ plane with a full computational domain.

coolant for a film cooling flow as well as unsteady three-dimensional flow structures. Hence, a full computational domain with periodic boundary conditions is used throughout the following computations.

The cases were first run for the steady-state solution. It took around 3000 iterations to reach convergence. After being switched to an unsteady-state simulation with the steady-state results as the initial solution, the simulation continued to run parallel on 8 processors with 16 GB memory on the cluster. The unsteady computations were stopped to check whether a statistically steady state was reached. After around 5000 time steps, the typical fluctuation was found. Beyond this time, the dominant frequency of the fluctuation became a time-invariant value. Then, data sampling for time statistics will be launched for more time steps to calculate the time-averaged results. It took three weeks of intensive parallel computing of 8 processors on the cluster to get one solution.

Comparison of Turbulence Models

The relative performance of the two variants of the DES models is shown in Fig. 8. The realizable k-ε-based DES model yielded a result closer to the experimental data. Both models did capture the jet liftoff, however, the Spalart–Allmaras-based DES model considerably underpredicted the effectiveness in the near hole region. Both of the DES models overpredicted in the far downstream region.

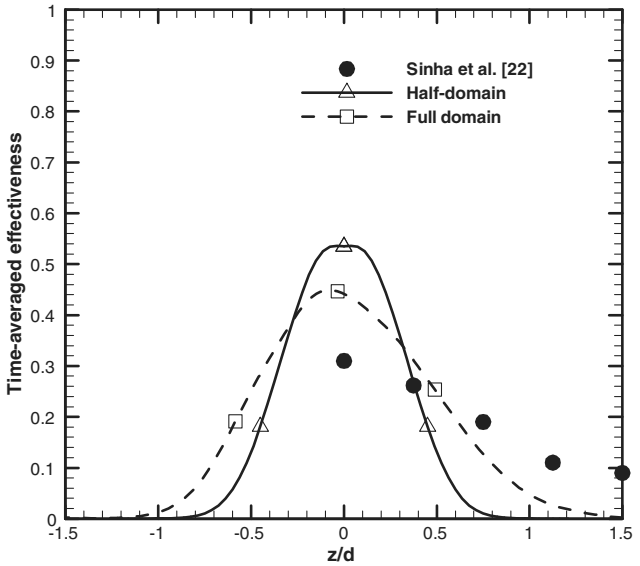

Fig. 7 Comparison of time-averaged spanwise effectiveness for different domains at $x/d = 15$.

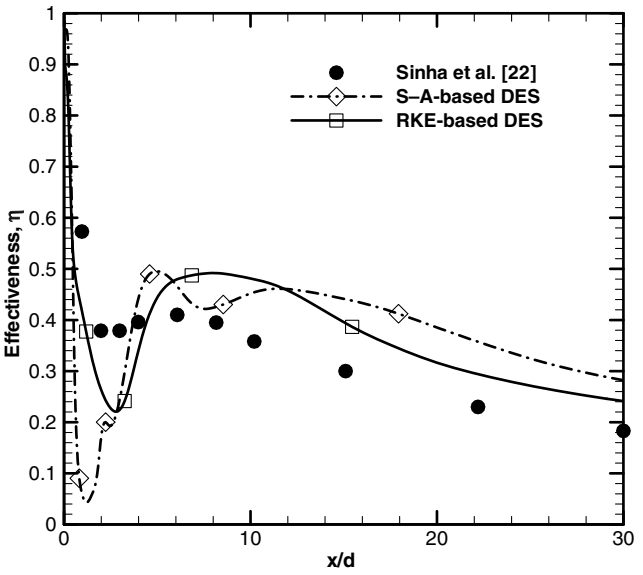

Fig. 8 Time-averaged film-cooling effectiveness along the centerline for different DES models.

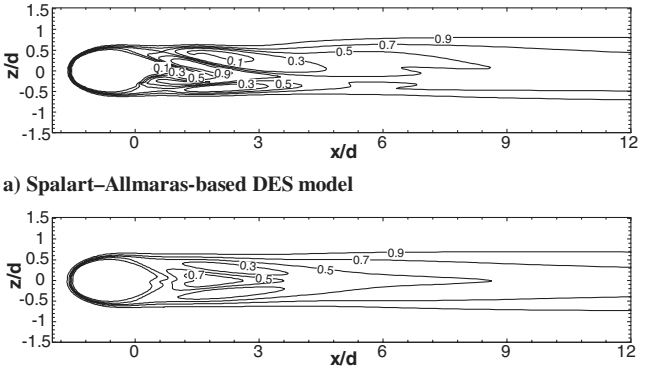

a) Spalart–Allmaras-based DES model

b) Realizable k-ε-based DES model

Fig. 9 Time-averaged temperature (θ) contours at $y/d = 0.1$ plane.

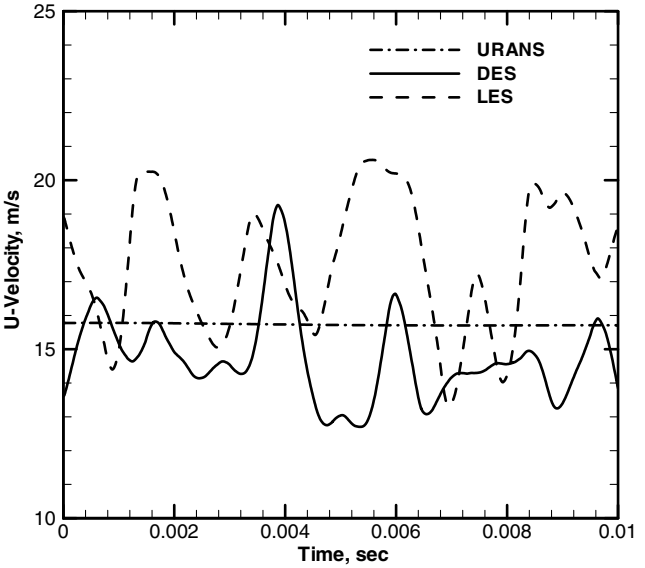

Fig. 10 An example of time-variant velocity at a point (7.5, 1.18, and 0.0 d) for different turbulence models.

Figure 9 shows the comparison between the time-averaged temperature distributions of different DES models. Although the instantaneous asymmetric distribution in the spanwise direction can be seen in both cases, the time-averaged results of the RKE-based DES model show a symmetric pattern in contrast to the result of S–A-based DES models. The asymmetric larger hot spot can be seen in the S–A-based DES simulation (Fig. 9a). This caused the excessive decrease of the centerline cooling effectiveness for the S–A-based DES simulation. Hence the realizable k-ε-based DES model is used throughout the following computations.

Unsteady simulations with different turbulence models, such as URANS (Unsteady RANS), DES, and LES are performed with the same mesh and time-step size for a direct comparison. All cases started from the same steady RANS solution (realizable k-ε model was used) as the initial data. A sample of monitored velocity time histories for each model are depicted in Fig. 10. The results of DES and LES show continuous velocity fluctuations for time variation, whereas the velocity of the URANS case approaches a constant value after a certain transient period. The vortical structures of each case can be seen in Fig. 11. URANS (realizable k-ε model was used) could not capture the unsteady vortical flow in this jet in a crossflow. Finally, the flowfield of the URANS simulation (Fig. 11a) and its film-cooling effectiveness (Fig. 12) become almost the same as the steady RANS results. DES and LES models show the unsteady vortical flow structures. The smaller eddies near the wall and the larger eddies in the outer region of the jet shear layer, depending on the grid scale, can be seen in the results of LES (Fig. 11c). Time-averaged film-cooling effectiveness of the LES case shows large variations near the injection hole due to the drastic eddies near the field of the coolant injection. In general, LES has to be run for a sufficiently long flow time with finer mesh to obtain stable statistics. However, in the present study, all cases of URANS, DES, and LES have been run with the same mesh for 4000 time steps (0.04 s) for time-averaged data after a transient period (about 5000 time steps). Thus, it can be attributed to insufficient mesh and computing time for LES. It can also be due to the constant inlet flow conditions, as the flow in LES depends highly on the inlet flow conditions [10]. To obtain accurate predictions using LES, the computational costs would be too extensive. In the DES prediction, only larger eddies in the outer region of the jet shear layer can be seen (Fig. 11b). The reason is that the flow in the near-wall region is simulated by the RANS approach. The LES and RANS regions in the DES case are illustrated in Fig. 13. The RANS region can be seen near the surface, and the other outer region is covered by LES. Far downstream, the

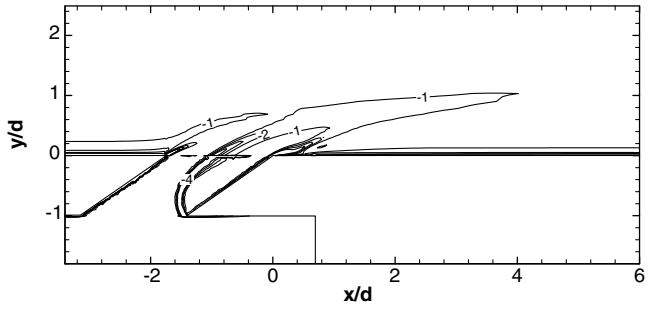

a) URANS

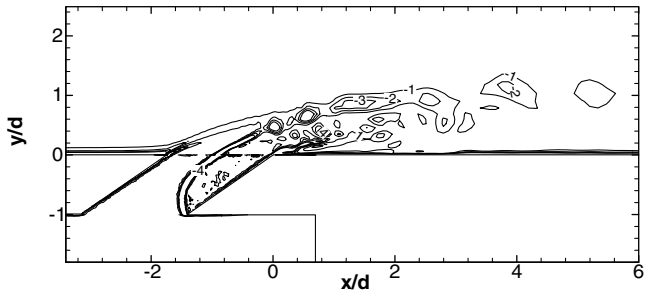

b) DES

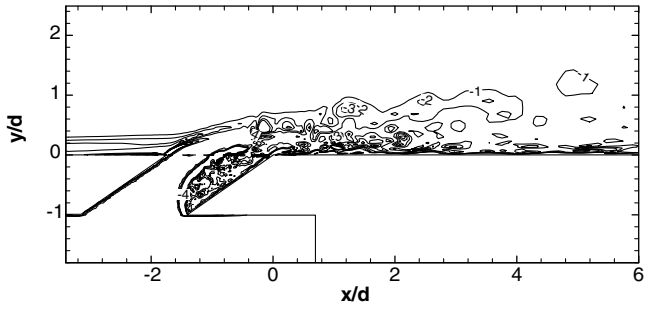

c) LES

Fig. 11 Instantaneous normalized vorticity ω_z contours at the center plane for different turbulence models.

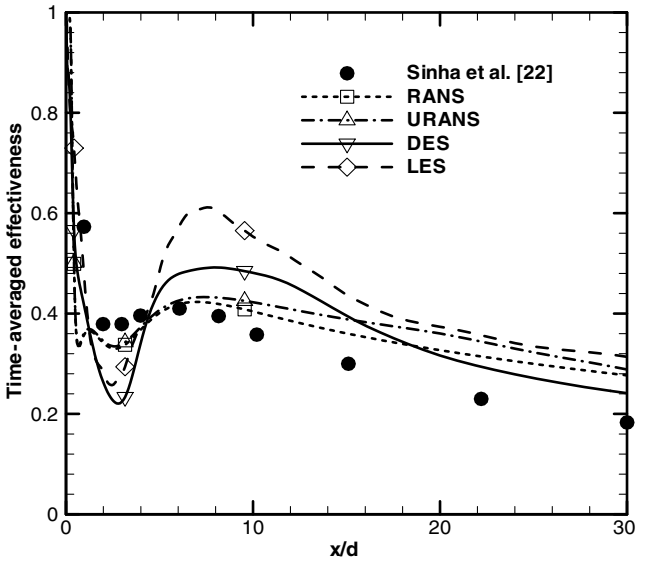

Fig. 12 Time-averaged film-cooling effectiveness along the centerline for different unsteady simulations.

turbulent mixing is almost accomplished, and the turbulent kinetic energy becomes low and the grid scale is relatively large, particularly above the wall boundary. Thus, the RANS region becomes large in the far downstream region (Fig. 13c) and has the shape of a larger coherent structure above the surface (Fig. 13b). Therefore, unsteady large-scale vortical flow structures (Fig. 11b) and efficient prediction of time-averaged film-cooling effectiveness (Fig. 12) can be achieved by using DES.

Comparison with Experimental Measurement

To validate the DES calculation procedure, the time-averaged DES results are compared with the film-cooling effectiveness data [22]. The time-averaged statistics are obtained from the run-time average from the computations over 8000 time steps. Many

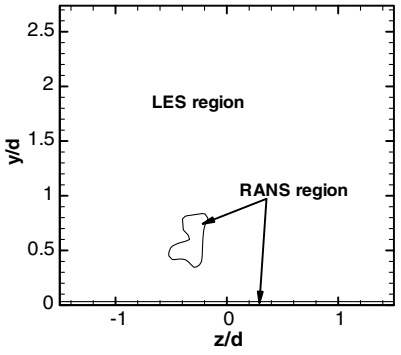

a) At x/d=5.0 plane

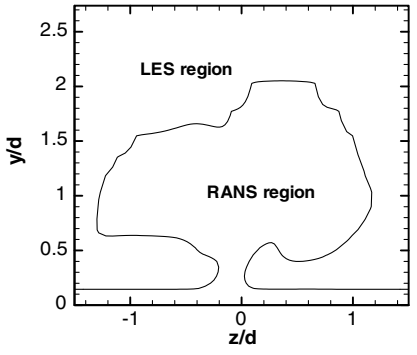

b) At x/d=15.0 plane

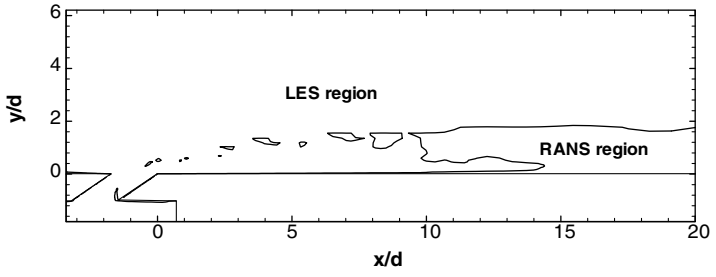

c) At center plane

Fig. 13 An example of the distributions of LES and RANS regions in DES computation.

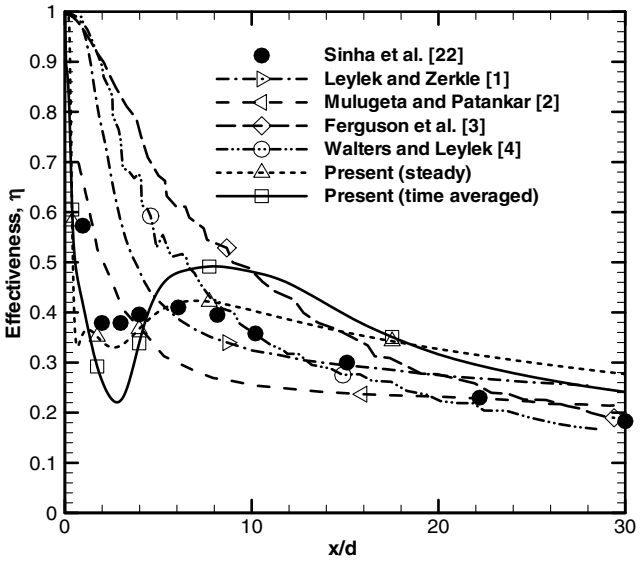

Fig. 14 Comparison between experimental and computational values of the film-cooling effectiveness along the centerline $z/d = 0$.

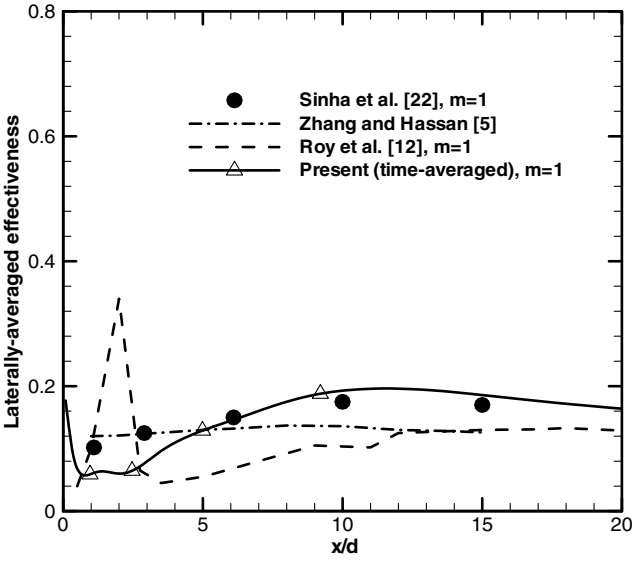

Fig. 15 Comparison between experimental and computational values of the laterally-averaged effectiveness.

researchers have compared their steady numerical predictions with the measurements of [22]. Their predictions agreed well with the experimental data at low blowing ratios, whereas the significant disagreement occurred near downstream of the jet exit at higher blowing ratios (e.g., 1), as shown in Fig. 14. At higher blowing ratios, the coolant jets will lift off from the surface and penetrate into the main stream, causing highly unsteady mixing. Most of the previous steady computational works failed to capture the jet liftoff phenomenon, and this was attributed to either the deficiency of the turbulence models, the use of isotropic eddy viscosity models, or the use of wall functions. However, the present steady (realizable k-ε model used) and DES predictions show the rapid decrease of cooling effectiveness near downstream of the injection hole due to the jet liftoff and hot entrainment flows. Details of the steady simulations can be found in [5].

The time-averaged distribution of the laterally-averaged film-cooling effectiveness with a 1.0 blowing ratio is shown in Fig. 15. Also shown are experimental data [22] and the other DES results [12] at the same blowing ratio. In both experiments and computations, the coolant delivery tube length is same and equal to 1.75 d. The unsteady vortical flow enhances the mixing process in the wake region and enlarges the mixing region. Also, the coolant spreads more in the spanwise direction for the unsteady time-averaged simulation than for the steady simulation. The present RKE-based DES simulation without the symmetric boundary conditions shows a more satisfactory agreement with the downstream experimental results. The jet liftoff behavior immediately downstream of the jet exit and the comparable agreement between the cooling effectiveness predictions and the experimental data can be obtained through unsteady DES simulations. However, there is still some discrepancy

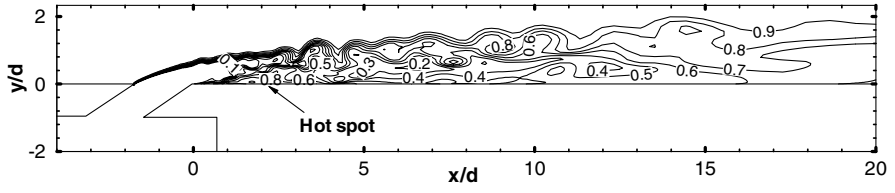

a) Instantaneous

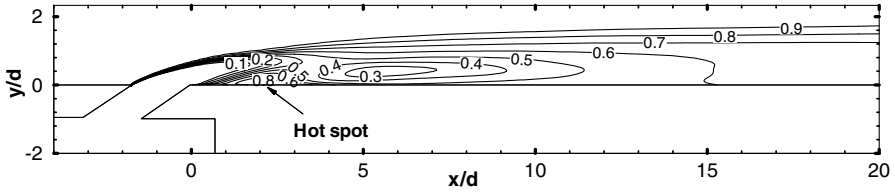

b) Time averaged

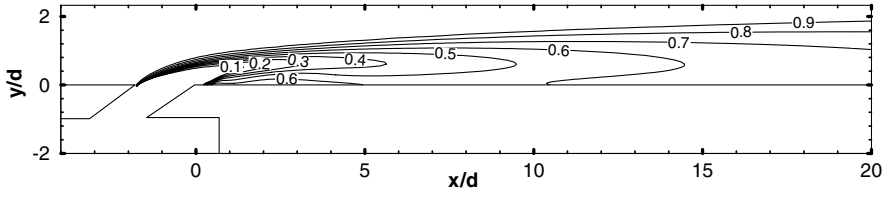

c) Steady

Fig. 16 Nondimensional temperature (θ) distributions at the center plane.

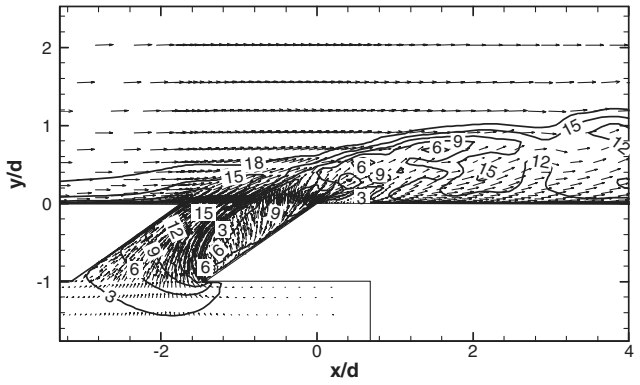

a) At z/d=0 plane

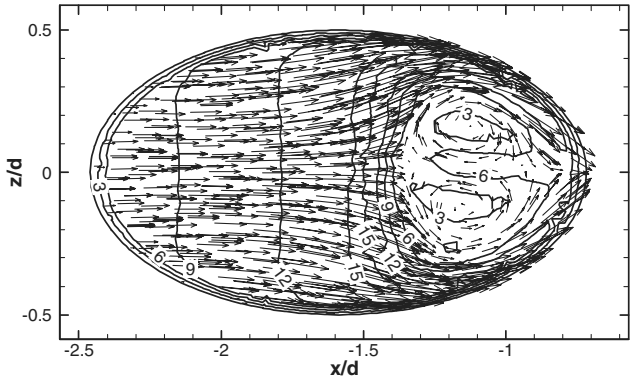

b) At the middle of tube

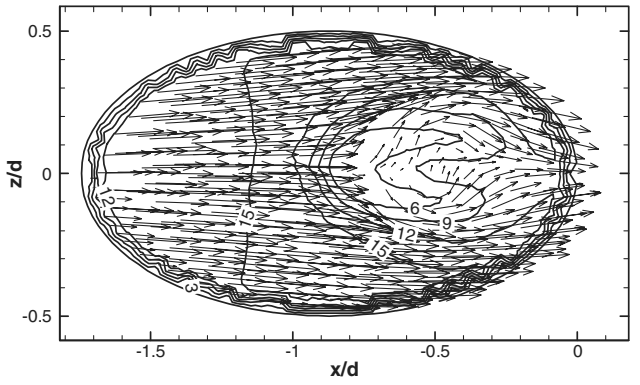

c) At the tube outlet

Fig. 17 Instantaneous velocity vectors and velocity magnitude (m/s) distributions in the coolant injection tube.

between them. To obtain a more accurate prediction, the improvements of the DES model and grid system as well as realistic inflow conditions are required.

Results

Coolant Jet Injection, Jet Liftoff, and Mixing Phenomena

The nondimensional temperature distribution (instantaneous, time averaged, and steady) in the wake region near downstream of the coolant jet injection is plotted in Fig. 16. The z coordinate of the planes in Fig. 16 is at the center plane $z/d = 0.0$. The instantaneous result reveals a highly unsteady mixing process, which is associated with jet liftoff behavior. The hot spot immediately downstream of the jet exit, caused by a coolant jet liftoff and hot entrainment flows, can be seen in both the instantaneous and the time-averaged temperature distributions (Fig. 16a and 16b), in contrast to the steady result (Fig. 16c).

In Fig. 17, the instantaneous velocity vectors and velocity magnitude distributions inside the coolant injection tube describe a flow structure in the tube. The instantaneous DES solution shows that most of the fluid is impinging with high velocity on the left half (windward) of the tube due to an inclined tube. In the right half (leeward), the entrained fluid is creating a small recirculation. We can see that the vortical flow structure in the coolant jet occurs from the middle of the tube (see Fig. 17b). Finally, at the exit plane of the tube, the flow is highly nonuniform (Fig. 17c). The relatively high-velocity coolant jet and the low-velocity vortical flow are issued from the tube and bend towards the mainstream direction. Figure 18 shows the instantaneous pressure distribution on the test surface around the injection hole. In Fig. 18, we can see the low pressure region immediately downstream of the injection hole, similar to the flowfield of a bluff body. This pressure distribution results in entrainment from the hot main stream on both sides of the coolant jet.

To illustrate the effect of the vorticity from the tube on the mixing jet and jet liftoff, instantaneous temperature contours and velocity vectors in spanwise planes along the streamwise direction are presented in Fig. 19. The beginning of the counter-rotating vortex pair (CVP) at both side edges of the coolant jet can be seen in Fig. 19a (at $x/d = 0.1$, immediately downstream of the coolant jet hole). Also, we can see other vortices (inner vortices) at the central region. These inner vortices make the wake region of the coolant jet more complicated. They also aid the hot entrainment flow to come and mix in the central region (see Fig. 19b at $x/d = 1.0$). In Fig. 19b (at $x/d = 1.0$) it is confirmed that the hot boundary layer exists immediately downstream of the jet hole for this blowing ratio, due to the coolant jet liftoff and hot entrainment flow (the measurement of [22] exhibited significantly low film-cooling effectiveness in this region). Around $x/d = 3.0$, the inner vortices issued from the coolant injection tube merged with the large counter-rotating vortex pair and disappeared (see Fig. 19c at $x/d = 3.0$).

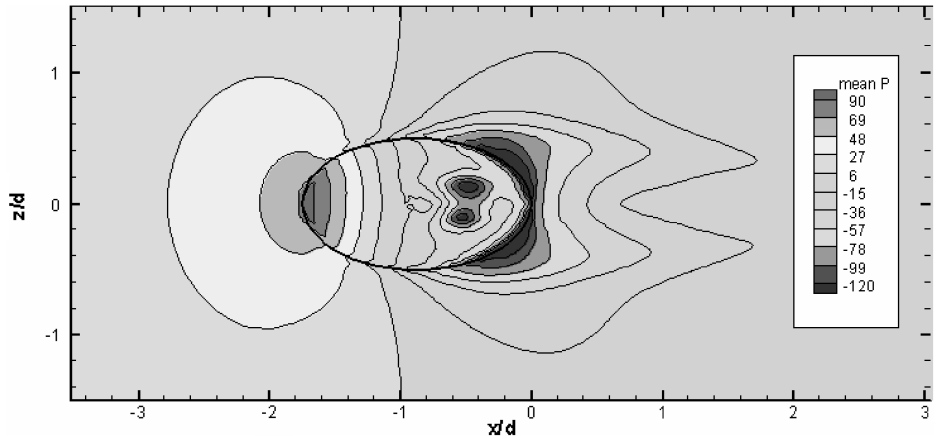

Fig. 18 Instantaneous pressure distribution on the test surface near the injection hole (gauge pressure, Pa).

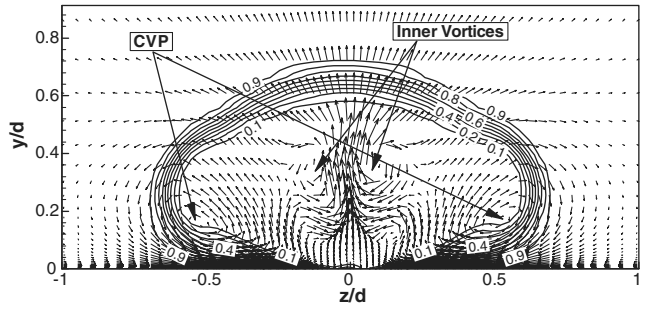

a) At x/d=0.1 plane

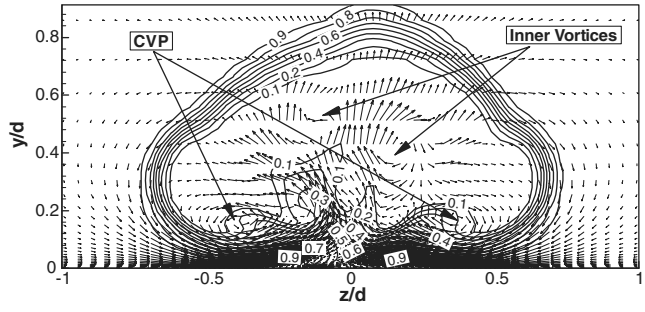

b) At x/d=1.0 plane

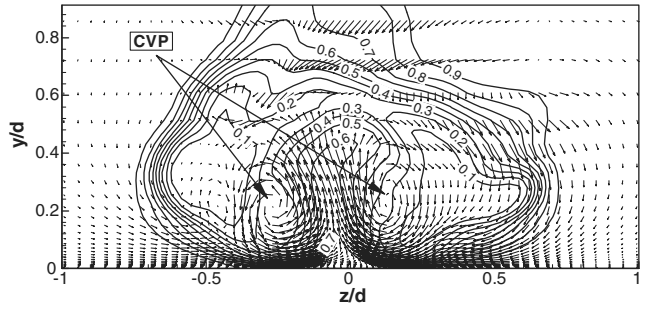

c) At x/d=3.0 plane

Fig. 19 Instantaneous temperature (θ) contours and velocity vectors in several spanwise planes.

To identify the turbulent frequency spectrum of the vortical structures and mixing phenomenon, fast Fourier transform (FFT) analyses are conducted using the time-variant velocity components (u, v, w) at different locations (using 8192 time-step data). The monitor points are shown in Fig. 20 and Table 1. The points (P1, P2) are located in the injection pipe and at the jet exit. The shear layer (P3, P4) between the main crossflow and the coolant jet along with the wake region (P5, P6) downstream of the jet exit are also monitored.

Figure 21 shows the FFT frequency spectra for the velocity components at these locations. For a vortical flow in the coolant pipe, caused by the deflected flowpath, distinct peaks of v and w can be observed for $f = 439$ Hz (see Fig. 21a). Defining a Strouhal number based on the pipe diameter and the mean value of coolant velocity results in a value of $Sr \approx 0.5$. The dominant frequency spectrum at

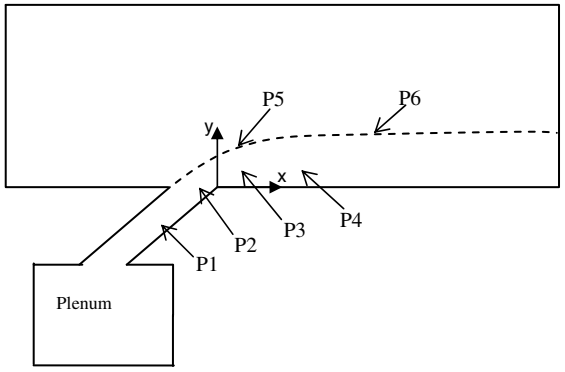

Fig. 20 Schematic of the monitoring points.

the points in the pipe region is concerned with the second resonance in a pipe flow $f = (n/2)(c/L)$ ($f \approx 449$ Hz for $n = 2$; $c =$ mean coolant jet velocity; $L = 1.75\ d$), whereas the turbulent noise is quite low. In the wake region near downstream of the jet exit (P3), the peak at 439 Hz is still pronounced, however, the turbulent fluctuations in the wake cause a broad band of peaks at lower as well as higher frequencies (Fig. 21b). Also, in the shear layer near the injection hole (P5), the dominant frequency occurs at 439 Hz. Further downstream in both the shear layer and the wake region (P4 and P6), different dominant frequencies are observed. Consequently, the frequency of the vortical flow in the injection pipe has an important role in the unsteady and mixing phenomena in the vicinity of the injection hole. Clearly, for this blowing ratio $m = 1$ and a combination of crossflows and coolant jet injection, the effect of the vorticity in the injection tube on the unsteady feature of this flow is not negligible but very significant. The different magnitude of each velocity component, shown in Fig. 21, supports the statement of anisotropic turbulence in the wake region.

Coherent Structures

The typical coherent structures for jets in crossflows reported in the literature are the CVP, the horseshoe vortex, the upright wake vortices, and the jet shear layer vortices. Most of these structures have been identified experimentally for normal jets injected at high blowing ratios, and the flow structures have been visualized using smoke-wire or dye-injection techniques [6,24]. There have been rare studies, either experimental or computational, that have reported on the flow structures associated with an inclined jet injected into a crossflow at a moderate blowing ratio.

To clearly observe the coherent structures of a jet in a crossflow, each normalized component of the vorticity field is presented at respective typical planes in Fig. 22. The spanwise vorticity component ω_z at $z/d = 0$ plane shows shear layers or roller vortices (negative vorticity patches) (Fig. 22a). One shear layer comes from the sharp edge in the coolant injection tube inlet. This represents that there are both high-speed flows and low-speed vortical flows in the tube. The roller vortices are shed regularly into the wake region and are convected downstream. Note that evidence of a weak horseshoe vortex is seen upstream of the inclined jet. A weak horseshoe vortex wrapping the base of a coolant jet issuing from a wall into a crossflow

Table 1 The monitored points and dominant frequencies

	Location	u component	v component	w component
P1 (in the tube)	(−1.18, −0.51, −0.22 d)	439 Hz		439 Hz[a]
P2 (tube outlet)	(−0.50, 0.0, 0.16 d)	439 Hz	439 Hz[a]	439 Hz
P3 (in the wake)	(1.0, 0.40, 0.14 d)	439 Hz[a]	439 Hz	439 Hz
P4 (in the wake)	(3.0, 0.39, 0.38 d)	439 Hz	854 Hz[a]	
P5 (shear layer)	(1.0, 0.76, 0.0 d)	439 Hz[a]		
P6 (shear layer)	(0.76, 1.18, 0.0 d)	513 Hz[a]	854 Hz	

[a] The highest amplitude component.

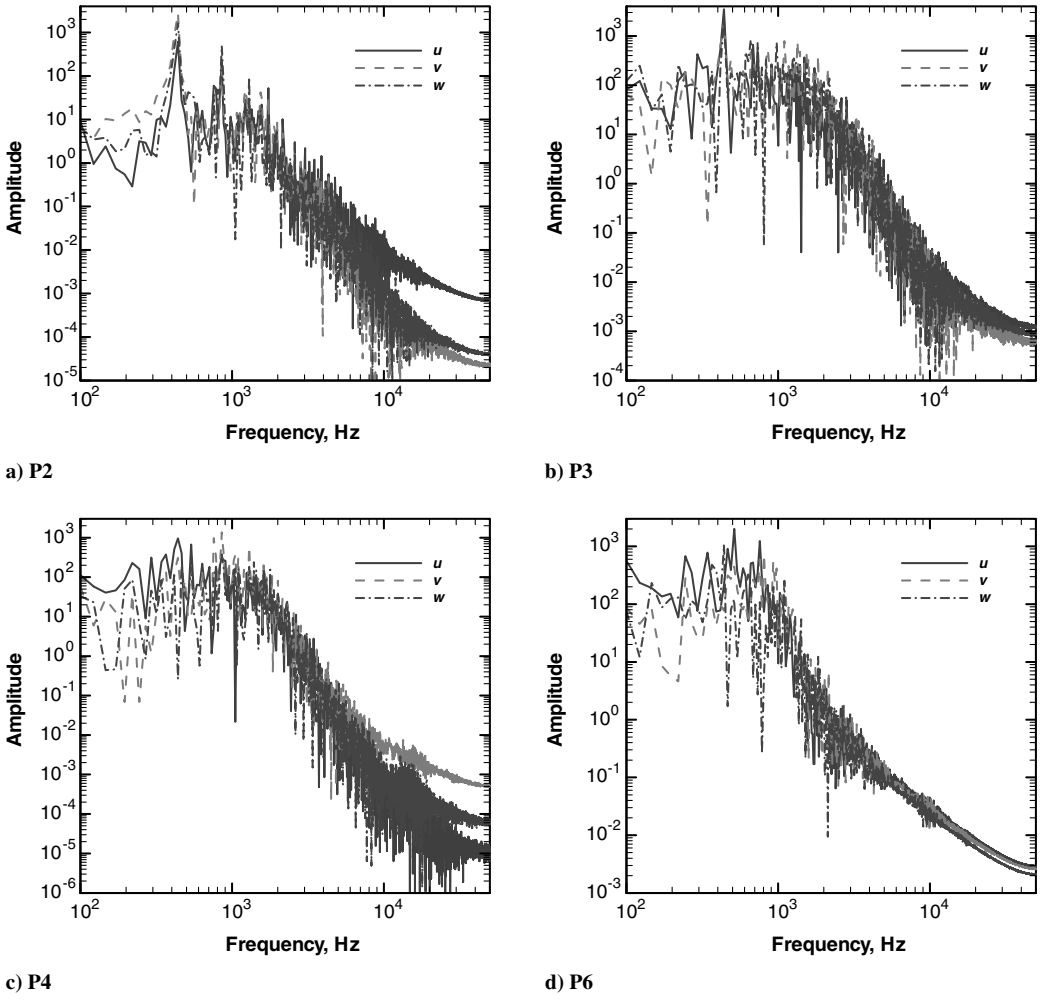

Fig. 21 FFT spectrum of time-variant velocity components (u, v, w) at several points.

is shown in Fig. 23. In Fig. 23a, a plan view of a horseshoe vortex is shown using a path line. It is entrained into the central region just downstream of the coolant jet. This hot entrainment flow and coolant jet liftoff cause the hot spot near downstream of the coolant jet. Figure 23b shows a cross-sectional view of a horseshoe vortex for the same flow (indicated by an arrow). However, a horseshoe vortex pair was not seen in the LES for the same flow [9] because the used grid (uniform grid of $172 \times 102 \times 62$ for the domain of $17 \times 5 \times 6$ d) is too large to capture this vortex near the wall.

To visualize the coherent structures in the wake region, the vertical component ω_y is presented at a plane above the surface ($y/d = 0.25$) in Fig. 22b. In the near-wake region, a symmetric vortex pair, with opposite vorticity on either side of the coolant jet, is observed. This is in contrast to the wake of a bluff body where the vortices are shed alternately on either side of the centerline. Complex coherent vortical structures are shown in the wake region. It is attributed to the entrainment and reorientation of the crossflow boundary layer and the inner vortices issued from the coolant jet injection in the wake region. Further downstream the wake vortices are less organized and seem to have spread outward in the spanwise direction.

The vorticity component ω_x in the spanwise plane is presented at $x/d = 1$ (Fig. 22c) to illustrate the development of the counter-rotating vortex pair. This coherent structure persists in the far field of the jet and is the only dominant organized pattern that can be observed in the time-averaged mean velocity field. The origin of the CVP is associated with the vorticity along the spanwise edges of the exiting coolant jet boundary layer.

The Q criterion was used to identify coherent structures. It indicates the balance between the rotation rate and the strain rate. Positive Q isosurfaces isolate areas where the strength of rotation overcomes the strain, making those surfaces eligible as vortex envelopes [25]. Thus, coherent structures can be more easily seen using positive isosurfaces of the Q criterion. In Fig. 24, the isosurface corresponding to a positive value of 2 is plotted and yields typical coherent structures, including a weak horseshoe vortex, CVP, vortex tube (inner vorticies) issued from the injection tube, and downstream hairpin coherent structures. The hairpin coherent structure is considered as the primary large-scale structure associated with the jet in a crossflow [9]. Based on the present simulations, the other various coherent structures identified in Fig. 24 are all related to the evolution, growth, and transport of the hairpin structures.

Conclusions

Unsteady simulations were performed for a simplified geometry representing film cooling of a gas turbine blade surface using a detached eddy simulation scheme. To obtain accurate results, time-step size, grid resolution, and computational domain tests are conducted. Unsteady simulations using URANS, DES, and LES are also performed. We can obtain better prediction using DES, which reveals both advantages of RANS and LES. A comparison of time-averaged DES predictions with experimental data from [22] shows the adequacy of the DES approach for film cooling flows. Unsteady large-scale vortical structures in a film cooling flow are explained in terms of instantaneous temperature contours, velocity vectors, and Q criterion. Typical coherent structures in this inclined jet in a crossflow are obviously depicted using isosurfaces of the Q criterion, and a horseshoe vortex, CVP, and roller vortices are identified. Through the frequency and vortical structure analysis, there is an attempt to show

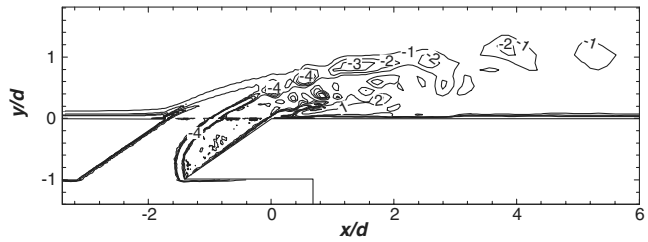

a) At z/d=0.0 plane

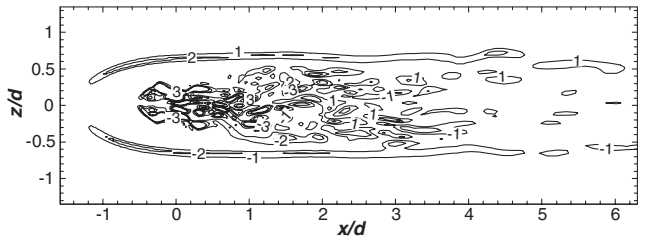

b) At y/d=0.25 plane

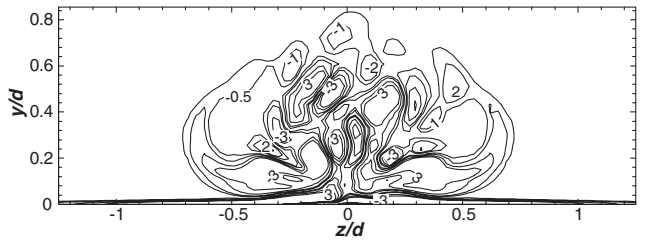

c) At x/d=1.0 plane

Fig. 22 Instantaneous normalized vorticity contours at projection planes.

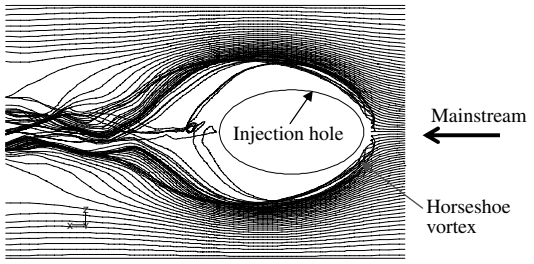

a) Plan view at the base

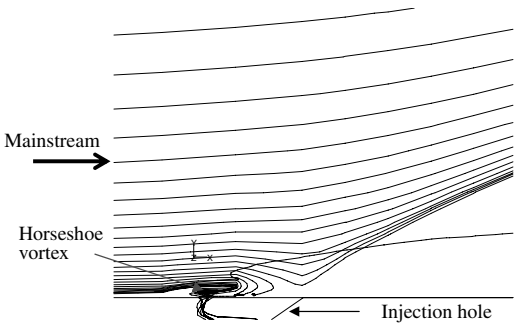

b) Center plane section

Fig. 23 Horseshoe vortex system near the wall (horseshoe vortex is indicated by arrow).

the relation between inner vortices (make vortex tubes) issued from the jet injection tube, mixing process, and jet liftoff phenomena. Further investigation of the interaction between the unsteady

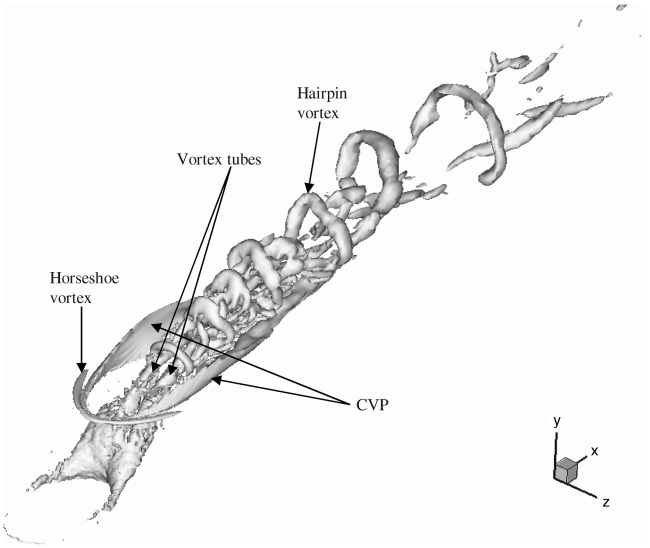

Fig. 24 Details of the coherent structures in the inclined jet in a crossflow.

coherent structures and the heat transfer characteristics are needed for various flow conditions.

References

[1] Leylek, J. H., and Zerkle, R. D., "Discrete-Jet Film Cooling: A Comparison of Computational Results with Experiments," American Society of Mechanical Engineers, Paper 93-GT-207, 1993.

[2] Mulugeta, K. B., and Patankar, S. V., "Numerical Study of Discrete-Hole Film Cooling," American Society of Mechanical Engineers, Paper 96-WA/HT-8, 1996.

[3] Ferguson, J. D., Walters, D. K., and Leylek, J. H., "Performance of Turbulence Models and Near-Wall Treatments in Discrete Jet Film Cooling Simulations," American Society of Mechanical Engineers, Paper 98-GT-438, 1998.

[4] Walters, D. K., and Leylek, J. H., "A Detailed Analysis of Film Cooling Physics: Part 1: Streamwise Injection with Cylindrical Holes," *Journal of Turbomachinery*, Vol. 122, No. 1, 2000, pp. 102–112. doi:10.1115/1.555433

[5] Zhang, X. Z., and Hassan, I. G., "Film Cooling Effectiveness of an Advanced-Louver Cooling Scheme for Gas Turbines," *Journal of Thermophysics and Heat Transfer*, Vol. 20, No. 4, 2006, pp. 754–763. doi:10.2514/1.18898

[6] Fric, T. F., and Roshko, A., "Vortical Structure in the Wake of a Transverse Jet," *Journal of Fluid Mechanics*, Vol. 279, 1994, pp. 1–47. doi:10.1017/S0022112094003800

[7] Bernsdorf, S., Rose, M. G., and Abhari, R. S., "Modeling of Film Cooling—Part I: Experimental Study of Flow Structure," *Journal of Turbomachinery*, Vol. 128, No. 1, 2006, pp. 141–149. doi:10.1115/1.2098768

[8] Hoda, A., Acharya, S., and Tyagi, M., "Predictions of a Jet-In-Crossflow with Reynolds Stress Transport Models and Large Eddy Simulations," American Society of Mechanical Engineers, Rept. IGTI00, Munich, 2000.

[9] Tyagi, M., and Acharya, S., "Large Eddy Simulation of Film Cooling Flow from an Inclined Cylindrical Jet," *Journal of Turbomachinery*, Vol. 125, No. 4, 2003, pp. 734–742. doi:10.1115/1.1625397

[10] Rozati, A., and Tafti, D. K., "Large-Eddy Simulation of Leading Edge Film Cooling: Analysis of Flow Structures, Effectiveness, and Heat Transfer Coefficient," *International Journal of Heat and Fluid Flow*, Vol. 29, No. 1, 2008, pp. 1–17. doi:10.1016/j.ijheatfluidflow.2007.05.001

[11] Spalart, P. R., Jou, W.-H., Strelets, M., and Allmaras, S. R., "Comments on the Feasibility of LES for Wings, and on a Hybrid RANS/LES Approach," *1st AFOSR International Conference on DNS/LES*, edited by C. Liu, and Z. Liu, Greyden Press, Columbus, OH, 1997, pp. 137–147.

[12] Roy, S., Kapadia, S., and Heidmann, J. D., "Film Cooling Analysis Using DES Turbulence Model," American Society of Mechanical Engineers, Paper GT-2003-38140, 2003.

[13] Martini, P., Schulz, A., Bauer, H.-J., and Whitney, C. F., "Detached Eddy Simulation of Film Cooling Performance on the Trailing Edge Cutback of Gas Turbine Airfoils," *Journal of Turbomachinery*, Vol. 128, No. 2, 2006, pp. 292–299. doi:10.1115/1.2137739

[14] Kim, J., Moin, P., and Moser, R., "Turbulence Statistics in Fully Developed Channel Flow at Low Reynolds Number," *Journal of Fluid Mechanics*, Vol. 177, 1987, pp. 133–166. doi:10.1017/S0022112087000892

[15] Wilcox, D. C., *Turbulence Modeling for CFD*, DCW Industries, La Cañada, CA, 1993.

[16] Lesieur, M., Comte, P., Lamballais, E., Metais, O., and Silvestrini, G., "Large-Eddy Simulations of Shear Flows," *Journal of Engineering Mathematics*, Vol. 32, No. 2/3, 1997, pp. 195–215. doi:10.1023/A:1004228831518

[17] Moin, P., "Numerical and Physical Issues in Large Eddy Simulation of Turbulent Flows," *JSME International Journal, Series B (Fluids and Thermal Engineering)*, Vol. 41, No. 2, 1998, pp. 454–463.

[18] Shur, M., Spalart, P. R., Strelets, M., and Travin, A., "Detached-Eddy Simulation of an Airfoil at High Angle of Attack," *Engineering Turbulence Modelling and Experiments 4*, Elsevier Science, Amsterdam, May 1999.

[19] Spalart, P. R., and Allmaras, S. R., "A One-Equation Turbulence Model for Aerodynamic Flows," AIAA 92-0439, 1992.

[20] Fluent, Software Package, Ver. 6.3, Fluent Inc., Lebanon, NH, 2006.

[21] Shih, T.-H., Liou, W. W., Shabbir, A., Yang, Z., and Zhu, J., "A New k-ε Eddy-Viscosity Model for High Reynolds Number Turbulent Flows—Model Development and Validation," *Computers and Fluids*, Vol. 24, No. 3, 1995, pp. 227–238. doi:10.1016/0045-7930(94)00032-T

[22] Sinha, A. K., Bogard, D. G., and Crawford, M. E., "Film-Cooling Effectiveness Downstream of a Single Row of Holes with Variable Density Ratio," *Journal of Turbomachinery*, Vol. 113, No. 3, 1991, pp. 442–449. doi:10.1115/1.2927894

[23] Spalart, P. R., "Young-Person's Guide to Detached-Eddy Simulation Grids," NASA CR-2001- 211032, 2001.

[24] Kelso, R. M., Lim, T. T., and Perry, A. E., "An Experimental Study of Round Jets in Crossflow," *Journal of Fluid Mechanics*, Vol. 306, No. 1, 1996, pp. 111–144. doi:10.1017/S0022112096001255

[25] Dubief, Y., and Delcayre, F., "On Coherent-Vortex Identification in Turbulence," *Journal of Turbulence*, Vol. 1, No. 1, 2000, p. 11.